Final Technical Report:

Electrochemically-Driven Phase Transitions in Battery Storage Compounds

Submitted to:

U.S. Department of Energy
Office of Basic Energy Sciences

Principal Investigator: Professor Yet-Ming Chiang (MIT)

Awardee: Massachusetts Institute of Technology

DOE Award No. DE-SC0002626

Period of Peformance:

9/15/2009 - 9/14/2020

Project Summary:

Compounds of interest for ion storage in advanced batteries frequently exhibit phase transformations as the working ion concentration varies. Under large electrochemical driving forces inherent to practical use, systems are often driven far from equilibrium. This program combines experiments and theory to understand the phase transition behavior of ion insertion compounds when electrochemically driven far from equilibrium. As model systems, we focus on alkaline metal phosphates *AM*PO4 (*A* = alkali; *M* = first row transition metal) of olivine structure, which are both technologically interesting and ideally suited for fundamental study due to the ability to systematically tune transformation strain, and along with it, the phase transformation pathway. Behavior in compositions having large transformation strains (~15 vol%) requiring plasticity for strain accommodation is emphasized. Experimental techniques include *operando* characterization of structure while simultaneously varying electrokinetic parameters, and high resolution microscopy of nanoscale and interfacial phenomena. Phase-field modeling is used to model the thermodynamics and kinetics of competing transformation pathways, extended to include the effects of plasticity, and integrated with porous electrode kinetic theory to treat multi-particle effects. Success in this project will lead to an ability to design ion storage compounds with predictable transformation pathways, electrochemical kinetics, capacity utilization, and durability. New technologically important compounds may also be discovered.

BACKGROUND

The importance of low-cost, high performance electrical energy storage to the US and the world is now widely recognized. This importance has become more significant in recent years by the need to accelerate deployment of electric vehicles and stationary storage for grid-connected and off-grid renewable energy. Amongst numerous storage technologies being explored, electrochemical storage (batteries) remains the most promising approach for meeting the energy density thresholds that will enable widespread adoption of electric transportation [1]. For stationary storage, after a period during the last decade where numerous alternatives (e.g., flywheels and compressed air) were also seriously considered and developed, advanced batteries have emerged as the dominant technology, an example being the California Public Utilities Commission's mandate to deploy 1.3GW of storage by 2020, equivalent to 5-6 GWh of batteries [2]. Although batteries are complex *systems* uniting many materials each with specific functions, the fundamental enabler of any battery system remains the storage electrodes (electrochemical couple) that define, through their physical properties, the voltage, capacity, energy, power, and life of the battery.

A unifying central theme that has emerged for the physical behavior of storage electrodes is that ion storage compounds are inherently used, and routinely driven, *far-from-equilibrium*. This is increasingly true with the drive towards new materials of higher storage capacity, power, and energy density. The fundamental reasons behind such demanding utilization are not difficult to appreciate. Consider, for example, that a Li-ion battery operates under *at least* a substantial driving force of 4 eV per Li^+ ion, and that the composition swings widely to exchange at least one out of every seven atoms (e.g., $Li_{0.5}CoO_2$, $LiFePO_4$, $LiMn_2O_4$) and as high as four out of every five atoms (e.g., $Li_{4.4}Si$). Smaller composition excursions are simply not interesting from a capacity/energy viewpoint. Furthermore, these large excursions in composition and high driving forces all are imposed at or near room temperature, often delaying or preventing approach to thermal equilibrium. Examples of far-from-equilibrium behavior include the solid-state-amorphization of Si upon initial lithiation at room temperature, which our group was the first to report [8]. All current examples of Si anodes including those recently reaching commercialization utilize the amorphous domain of behavior. Other materials in which

nonequilibrium behavior has been elaborated in detail include $LiFePO_4$, the prototypical phospho-olivine cathode, in which the thermodynamically preferred first-order phase transition is circumvented in various ways under dynamic use conditions, including solid solution or noncrystalline disorder transformations [3-7,9-12]. Consequently, olivine materials represented an ideal research platform for this project due to the prevalence of nonequilibrium behavior with emergence of new compositions and phases.

Our goal of achieving fundamental understanding of the far-from-equilibrium behavior of solids under electrochemical driving forces directly addressed a Grand Challenge in the 2007 Grand Challenges report [14] stated as: "How do we characterize and control matter away - especially very far away - from equilibrium?" The work performed also falls squarely within two of the main themes identified in the 2015 Grand Challenges study [15]. These are: "Mastering Hierarchical Architectures and Beyond-Equilibrium Matter" and "Beyond Ideal Materials and Systems: Understanding the Critical Roles of Heterogeneity, Interfaces and Disorder."

This Final Technical Report is organized chronologically by four periods of performance: 9/15/2009 - 9/14/2012, 9/15/2012 – 9/14/2015, 9/15/2015 – 9/14/2018, and a no-cost extension over the period 9/15/2018 – 9/12/2020.

Period of Performance 9/15/2009 - 9/14/2012

During this period of performance, we used phase field modeling and *in-situ* synchrotron X-ray diffraction to study electrochemically-driven phase transitions in the $Li_x(Mn_yFe_{1-y})PO_4$ system, with emphasis on the role of particle size and overpotential on the phase transition pathway. This composition system allows systematic exploration of phase space by varying lithium concentration (e.g., with electrochemical cycling) as well as Mn/Fe ratio. Large excursions in unit cell volume can occur during cycling, since the equilibrium misfit strain between fully lithiated and fully delithiated phases in the pure endmembers varying from ~6.5 vol% in $LiFePO_4/FePO_4$ to ~11 vol% in $LiMnPO_4/MnPO_4$. For mixed Mn/Fe compositions, an intermediate crystalline phase of with some Li solid solution also appears. We previous showed that reduction of crystallite size below 100nm reduces the Li miscibility gap [16], and correlated the accompanying reduction in transformation strain with facile phase transition behavior allowing high power [17,18]. Furthermore, combined theoretical-experimental studies under present DOE support showed that simple crystalline-crystalline transitions between coexisting equilibrium phases are the exception rather than the rule, with the appearance of metastable amorphous (or at least highly disordered) phases being common.

Results in the Li_xFePO_4 system can be understood in the context of the phase transition map in Figure 1a, developed from a diffuse-interface (phase-field) model in which the nucleation energy barriers associated with the crystalline-to-crystalline and crystalline-to-amorphous transitions are calculated as a function of the overpotential, particle size and misfit strain . In this model, the delithiated amorphous phase has lower surface energy than its crystalline counterpart. Starting with fully lithiated $LiFePO_4$, the preferred phase transition upon delithiation (charging) is shown as a function of particle size and overpotential. The amorphous-phase nucleation activation-energy decreases with particle size; and, during charging, this nucleation barrier decreases with increasing overpotential, $\Delta\phi$. The results, calculated using materials parameters appropriate to Li_xFePO_4, predicted that a crystalline-to-amorphous phase transition is preferred (i.e., has a smaller activation energy) above a critical value of overpotential, $\Delta\phi_{crit}$, which at large particle sizes is calculated to be ~20 mV (equivalent to an undercooling of ~230K for a thermal phase transition). The model predicts that $\Delta\phi_{crit}$ decreases with particle size, and vanishes below a critical size of about 70 nm, making the crystalline to amorphous transition the preferred one.

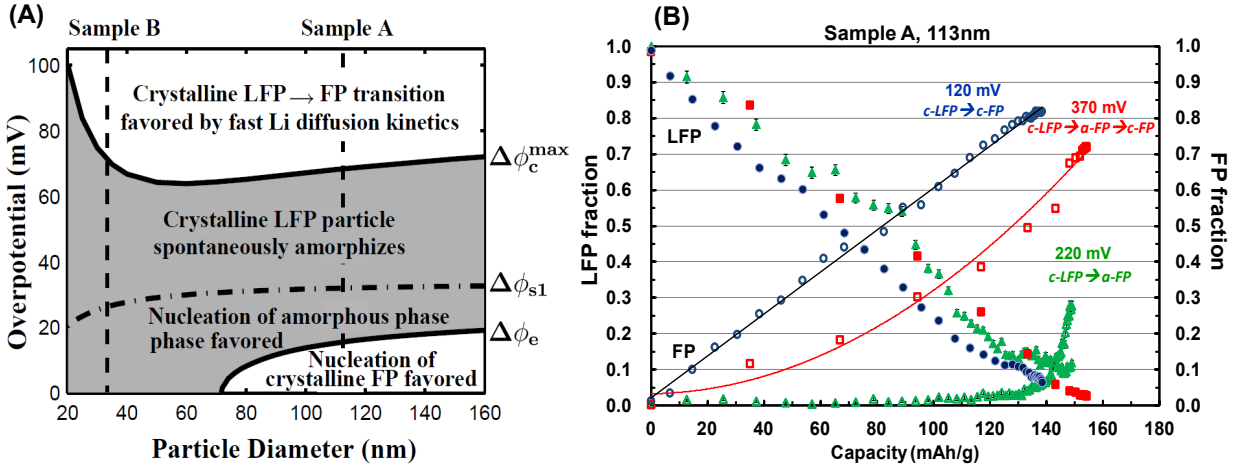

Figure 1. (a) Phase transition map calculated from a phase-field model, showing the preferred phase transition pathways upon delithiation of a crystalline LFP particle as a function of the overpotential , $\Delta\phi$, and particle size. Results are calculated for 2% linear misfit strain, appropriate to crystalline

$LiFePO_4$ (LFP) and $FePO_4$ (FP). The nucleation barrier for the crystalline-to-amorphous phase transition becomes smaller than that for the conventional crystalline phase transformation at $\Delta\phi > \Delta\phi_e$, and vanishes at $\Delta\phi_{s1}$, permitting spontaneous amorphization. Growth of the crystalline FP phase becomes preferred at $\Delta\phi > \Delta\phi_c^{max}$ due to Li diffusion-limited crystallization that is faster than the rate of structural disordering. Samples A and B correspond to experimental samples. (b) *In-situ* synchrotron X-ray diffraction results for Sample A, 113 nm mean particle size, show phase evolution upon potentiostatic charging at three different overvoltages (the overpotential range, obtained upon subtraction of cell polarization, corresponds to the left figure [19]).

However, an additional prediction of the model is another critical overpotential, $\Delta\phi_c^{max}$ above which the crystalline-to-crystalline phase transition pathway is again preferred. $\Delta\phi_c^{max}$ is a predicted upper bound to the overpotential at which amorphization is preferred. In contrast to supercooled thermal phase transitions, under electrochemical driving force the kinetics does not have a similar decrease with increasing driving force; at overpotentials greater than $\Delta\phi_{s1}$ in Fig. 1a, nucleation of the amorphous phase is expected to become very facile, and its *growth* may become rate-limiting. In contrast to the crystalline-crystalline transformation where the relative atomic positions are fixed, the crystalline LFP to delithiated amorphous transition requires coupled lithium diffusion and structural disordering at the growth front. The model includes competing kinetic processes whereby a higher overpotential generates a larger Li^+ out-flux from the particles while having no direct effect on the structural disordering kinetics. Thus at sufficiently large overpotentials, the structural disordering process becomes slow compared to lithium diffusion, and the direct crystalline phase transformation, which can be accommodated by lithium diffusion alone, reemerges as the preferred transition.

The prediction that the crystalline-crystallline transition is preferred at low and high overpotential, and amorphization at intermediate values, was borne out by *in-situ* synchrotron X-ray diffraction experiments conducted under potentiostatic charge (Fig. 1b), in which the crystalline LFP fraction decreases linearly with Li concentration at all applied potentials, but crystallization of FP is greatly suppressed at intermediate overpotential (green curve) compared to either lower (blue) or higher (red) overpotential. An even more dramatic demonstration of this phenomenon appears in Fig. 2, where galvanostatic of $LiFePO_4$ having particle sizes corresponding to Samples A and B in Fig. 1a undergo nearly complete amorphization. The structure of the electrochemically produced amorphous phase is not yet known; we propose to characterize such samples using pair distribution function analysis.

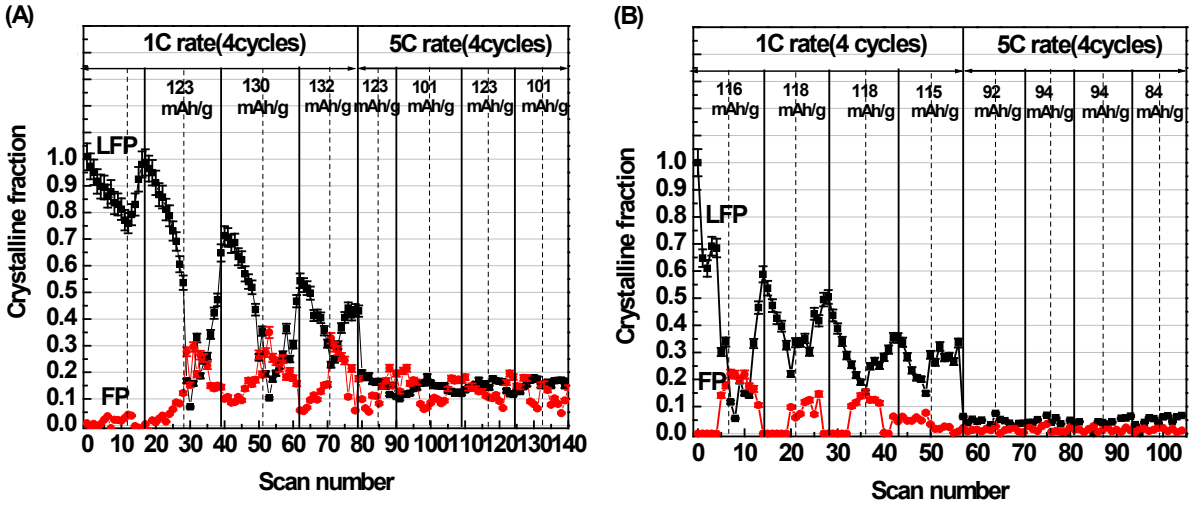

Figure 2. *In-situ* synchrotron XRD measurement of phase fractions for two $LiFePO_4$ materials during galvanostatic cycling at 1C rate for four cycles followed by 5C rate for four cycles. (A) Sample A of 113nm mean particle size; and (B) Sample B of 34nm mean particle size. Both show oscillating but decreasing LFP and FP crystalline fractions during 1C cycling, which however diminish sharply upon 5C cycling, showing that it is primarily the transformed amorphous phase that is being cycled at the higher rate.

We subsequently turned our attention to a mixed transition metal system, $Li(Mn,Fe)PO_4$, which is of interest for several reasons. The endmember $LiMnPO_4$ has a potential of 4.0V vs. Li/Li^+ compared to 3.45V for $LiFePO_4$, and therefore has substantially higher energy density as a battery cathode, but also has exceedingly slow charge-discharge kinetics which have prevented its commercial use. However, with even modest Fe additions, nanoscale $Li(Mn,Fe)PO_4$ exhibits the *highest* rate capability of all the olivines, $LiFePO_4$ included (see Fig. 6). The experimental and calculated phase diagrams for $Li(Mn,Fe)PO_4$ (Figs 3a and 3b) both contain an intermediate crystalline phase that has a range of Li solid solution, the quantitative details of which differ between experiment and theory. For a composition such as $LiMn_{0.5}Fe_{0.5}PO_4$, a section through Fig. 3b shows that at room temperature, three crystalline phases are expected with varying Li content (i.e., during charging and discharging), as shown in Fig. 3c. Electrochemically, two voltage "plateaus" corresponding to the Fe^{2+}/Fe^{3+} and Mn^{2+}/Mn^{3+} couples are seen in Fig. 3d, the transition between which lies within the solid solution range of the intermediate phase. Upon charging and discharging a cathode of such composition, simple first-order phase transitions between the lithiated and delithiated endmembers and the partially-lithiated intermediate phase are theoretically expected. However, our experiments revealed behavior far from this ideal picture.

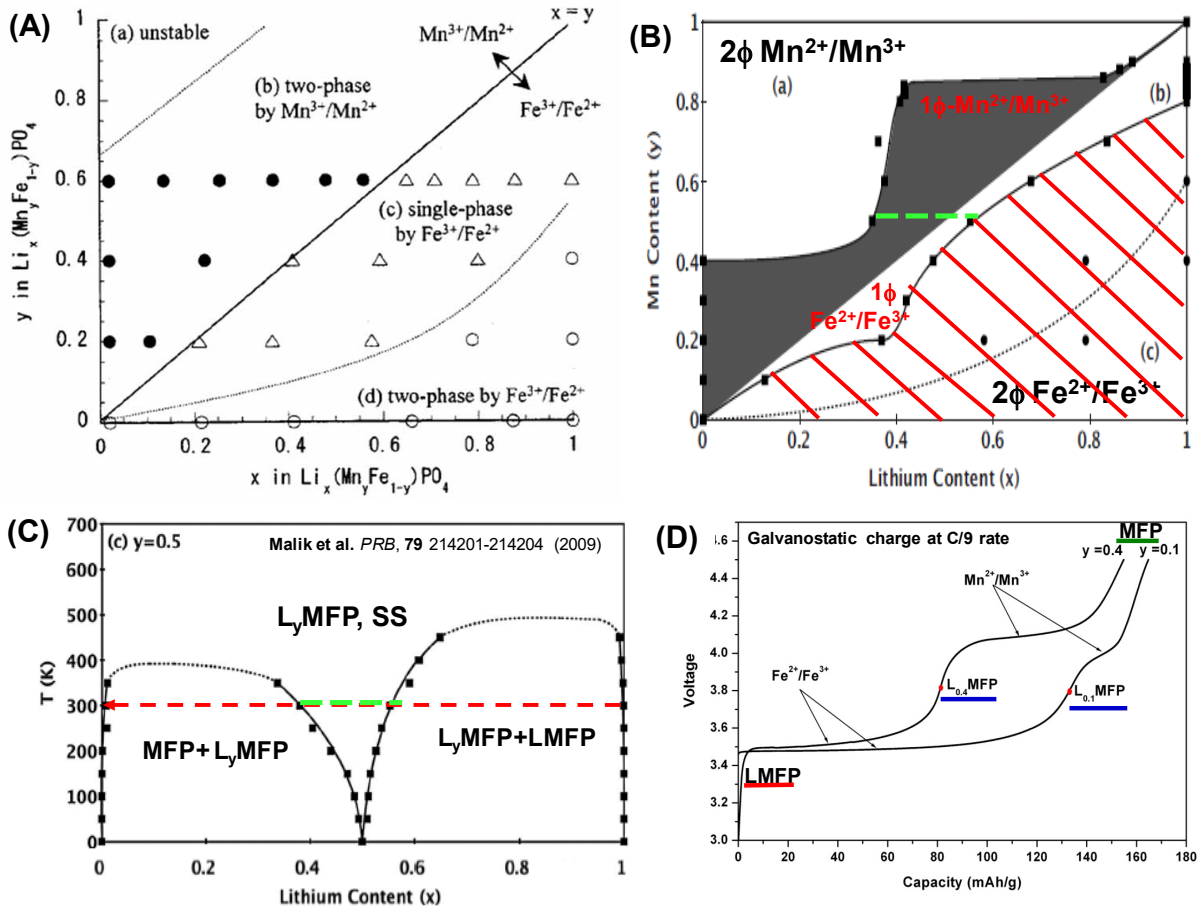

Figure 3. (A) Experimental; and (B) computed phase diagrams for $LiMn_yFe_{1-y}PO_4$ showing existence of intermediate single-phase field. (refs: Yamada et al. *JECS*, 148(10) A1153-A1158 (2001) and Malik et al. *PRB*, 79 214201-214204 (2009)) (C) Computed temperature – lithium concentration phase diagram for $Li_xMn_{0.5}Fe_{0.5}PO_4$ from Malik et al.; and (D) experimental voltage vs. capacity curves for $LiMn_yFe_{1-y}PO_4$ at y = 0.4 and 0.1, measured at C/9 galvanostatic current, this work.

In-situ X-ray diffraction experiments were conducted at beam line X-14A at Brookhaven National Laboratory (BNL) using transmission cells designed and fabricated at MIT. Data was collected during charging/discharging at galvanostatic rates up to 1C (1h for complete charge or discharge), and during potentiostatic experiments where the cell voltage was raised to desired values and held while the evolution of phases was monitored vs. time. Figure 4 shows typical results for a galvanostatic experiment. Here a $LiMn_{0.4}Fe_{0.6}PO_4$ powder of 50nm mean particle diameter (as determined from BET specific surface area measurements) was charged at a 1C rate while diffraction data were collected. In Fig. 4a, each of the spectra is labeled at with the charge capacity (in mAh/g) from the start of the experiment to the upper cutoff voltage of 4.5V (at 140 mAh/g, which is 82% of the theoretical capacity of 170 mAh/g). The vertical red arrows indicate the expected 2θ position of the three equilibrium crystalline phases shown in Fig. 3: We use the notation ”LMFP” for the fully lithiated endmember, “L_yMFP” for the intermediate compound of ~$Li_{0.4}$ composition, and the “MFP” for the fully delithiated endmember. One striking result is that the MFP phase never appears in this experiment, even at the end of charge when the composition is clearly in its two-phase coexistence field. A second result is

that during charging on the Fe^{2+}/Fe^{3+} plateau, where the equilibrium phase diagram indicates co-existence of LMFP and L_yMFP, the second of these crystalline phases doesn't form at all until a capacity of ~84 mAh/g is reached, indicated by the horizontal red dashed line in Fig. 4. Charging does not produce a nonequilibrium solid solution of the starting LMFP – this is clear from the unchanged LMFP peak position. As its intensity decreases, no new crystalline phase appears, suggesting the formation of amorphous phase as in nanoscale $LiFePO_4$. Crystallization of the equilibrium coexisting phase L_yMFP is only detected only above about 4.05V cell voltage of about 4.05V, which is well above the plateau voltage of ~3.6V. Upon further charging onto the Mn^{2+}/Mn^{3+} plateau at 4.2-4.4V, there is a *complete absence* of crystallization of the equilibrium MFP phase. Mass balance requires formation of another phase not detected by X-ray diffraction.

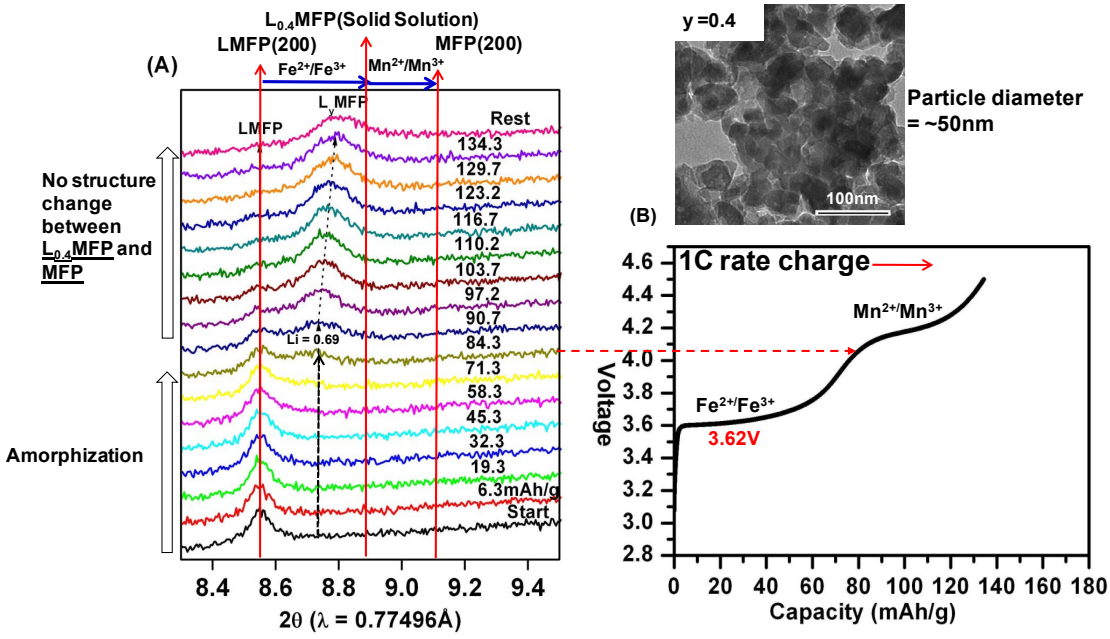

Figure 4. *In-situ* X-ray diffraction results obtained during galvanostatic charge at 1C rate of a nanoscale $LiMn_{0.6}Fe_{0.4}PO_4$ powder.

Galvanostatic cycling produces relatively low overpotentials in well-formulated electrodes of low resistance. We accessed higher overpotentials by conducting potentiostatic experiments. Figure 5 shows the same cathode material as in Fig. 4, now charged in two separate experiments by applying potentiostatic voltages of 4.0V (Fig. 5a) and 4.5V (Fig. 5b), respectively. During 4.0V charging, where the overpotential is well above the 3.6V plateau, the intermediate phase L_yMFP crystallizes as the starting LMFP phase diminishes – approximating the phase relationship expected from the binary lever rule. During 4.5V charging, the equilibrium crystalline phase MFP now finally appears ((the intermediate L_yMFP phase also appears, then disappears, as charge proceeds). Thus we induce crystallization of the MFP phase by the immediate application of a high overpotential, whereas this phase did not crystallize at all in the galvanostatic experiment, even when charging to the same final voltage of 4.5V. *This is the most striking and clear evidence for the critical role of overpotential in inducing phase crystallization that we have seen, and makes the LMFP system an ideal model for further study.*

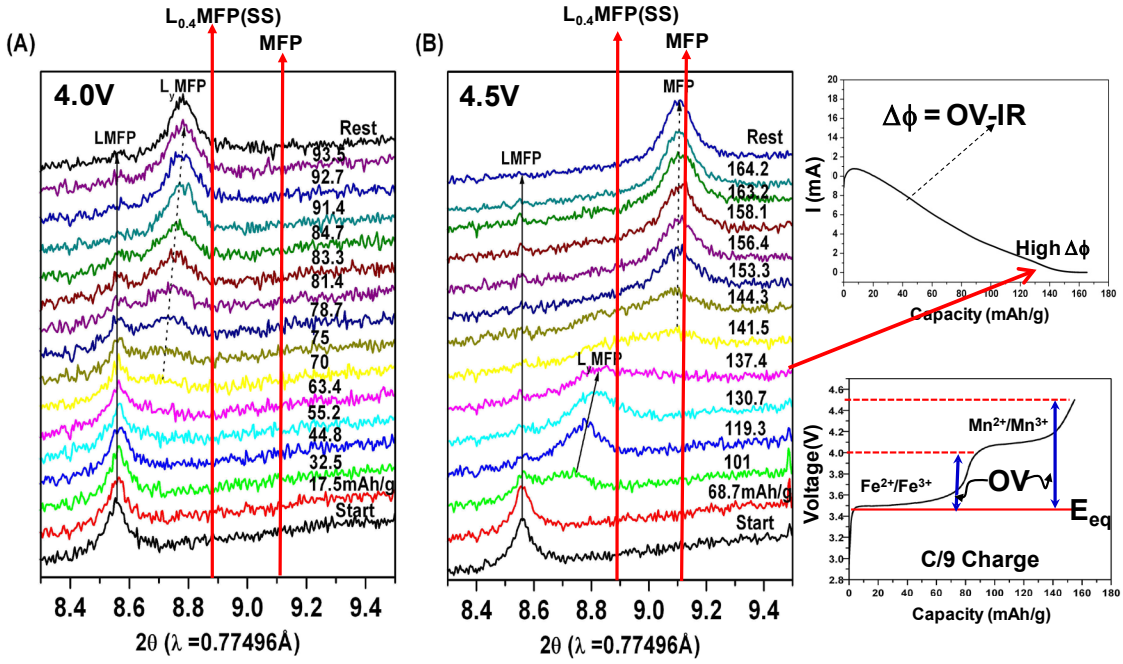

Figure 5. *In-situ* X-ray diffraction results obtained during potentiostatic charging at (A) 4.0V and (B) 4.5V of a nanoscale $LiMn_{0.6}Fe_{0.4}PO_4$ powder.

The behavior during *discharge* (lithiation) also differs from that seen during charge. For galvanostatic discharge at 1C rate with a small underpotential (Fig. 6), the relatively sharp crystalline "$Li_{0.4}$MFP" peak formed during charge (Fig. 3) first shifts position, indicating a nonequilibrium solid solution beyond the limits in both the experimental and calculated phase diagrams. At the end of discharge, what remains is a broad single peak located between the positions of the equilibrium phases LFMP and $L_{0.4}$MFP that suggests locally varying Li concentration. This asymmetry in behavior between charge and discharge also remains to be understood. We also do not know yet if high *underpotentials* during discharge will induce crystallization of the equilibrium compositions; this is an objective in the proposed work. Nonetheless, our results already provide insight into a technologically important observation that has been unexplained to this point. As shown in Fig. 6 (right), at high discharge rates between 10C and 50C (6 min to 72 sec discharge times), nanoscale $Li(Mn,Fe)PO_4$ olivines have exceptionally good capacity retention, even better than the nanoscale $LiFePO_4$ endmember shown for comparison. We believe this result can be explained by having reduced misfit strain during each step of the two-stage transformation, first between MFP and L_yMFP, then between L_yMFP and LMFP, avoiding a single transformation of large misfit strain. It is interesting to speculate that similar multistep transitions may allow the retention of high power in solid solutions containing still higher voltage components, such as $LiCoPO_4$ (4.8V) and $LiNiPO_4$ (5.4V) that further increase energy density.

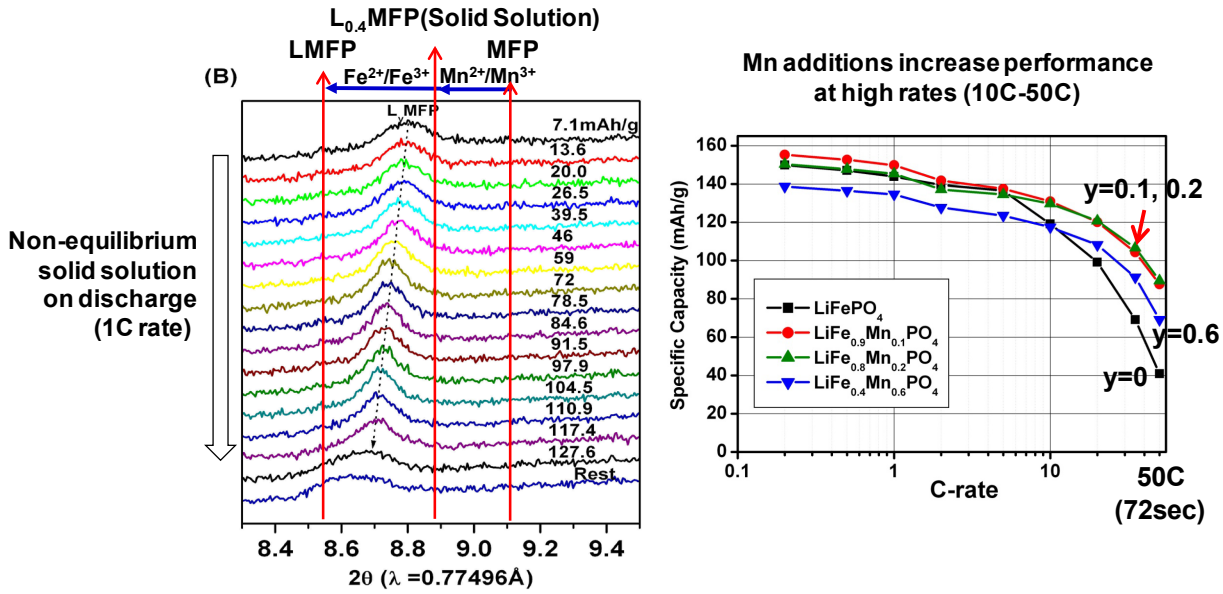

Figure 6. (Left) Galvanostatic discharge at 1C rate of a nanoscale $LiMn_{0.6}Fe_{0.4}PO_4$ cathode produces non-equilibrium solid solutions of the intermediate crystalline phase of nominal composition "$Li_{0.4}MFP$." (Right) Comparison of capacity vs. C-rate for nanoscale $LiFePO_4$ and $Li_{1-x}Fe_{1-y}Mn_yPO_4$ (y = 0.1, 0.2, 0.6). High rate capability in $Li_{1-x}Fe_{1-y}Mn_yPO_4$ is attributed to reduced misfit strain in the two-step transition between crystalline phases.

Several other practical consequences may be considered as a result of the overpotential-dependent phase transition behavior. For example, applications such as hybrid or all-electric vehicle batteries have charge/discharge protocols that produce frequent voltage transients, and thus varying overpotentials; these may produce unexpected and history-dependent phase states. Phase-state hysteresis could have consequences for *in-situ* monitoring of state-of-charge (SOC), impedance growth, storage kinetics, and battery durability due to electrochemical-mechanical coupling. In-depth knowledge of overpotential-and time-dependent phenomena could permit phase states and transition pathways to be electrochemically programed during pre-conditioning or operation of batteries.

References

1. DOE ARPA-E Energy Innovation Summit Presentation, “Going Places: Prospects for Transportation Alternatives”, available at http://arpa-e.energy.gov/sites/default/files/.
2. California Public Utilities Commission Press Release, available at http://docs.cpuc.ca.gov/PublishedDocs/Published/G000/M079/K171/79171502.PDF
3. Tang, M., Carter, W. C., Chiang, Y.-M., *Annu. Rev. Mater. Res*. 2010, 40, 501.
4. Tang, M., Carter, W.C., Belak, J.F., Chiang, Y.-M., *Electrochemica Acta* 2010, 56, 769..
5. Kao, Y.-H., Tang, M., Meethong, N., Bai, J., Carter, W.C., Chiang, Y.-M., *Chem. Mater*. 2010, 22, 5845.
6. Ravnsbæk, D. B., Xiang, K., Xing, W., Borkiewicz, O. J., Wiaderek, K. M., Gionet, P., Chapman, K. W., Chupas, P., Chiang, Y.-M., *Nano Lett.* 2014, 14, 1484.
7. Niu, J., Kushima, A., Qian, X., Qi, L., Xiang, K., Chiang, Y.-M., and Ju Li, *Nano Lett.* 2014, 14, 4005.
8. Limthongkul, P., Jang, Y.-I., Dudney, N.J., Chiang, Y.-M., *Acta Mater.* 2003, 51, 1103.
9. Meethong, N., Kao, Y.-H., Tang, M., Huang, H.-Y., Carter, W.C., Chiang, Y.-M., *Chem. Mater*. 2008, 20, 6189.
10. Meethong, N., Kao, Y.-H., Speakman, S.A., Chiang, Y.-M., *Adv. Funct. Mater.* 2009, 19, 1060.
11. Tang, M., Huang, H.-Y., Meethong, N., Kao, Y.-H., Carter, W.C., and Chiang, Y.-M., *Chem. Mater.* 2009, 21, 1557.
12. Liu, H., Strobridge, F.C., Borkiewicz, O.J., Chapman, K.W., Chupas, P.J., and Grey, C.P., *Science* 2014, 344, 1252817.
13. Malik, R., Zhou, F., Ceder, G., *Nature Mater.* 2011, 10, 587.
14. Hemminger, John, Graham Fleming, and M. Ratner. "Directing Matter and Energy: Five Challenges for Science and the Imagination." Department of Energy’s Office of Science (http://science. energy. gov/~/media/bes/pdf/reports/files/gc_rpt. pdf) (2007).
15. DOE Basic Energy Sciences Advisory Committee (BESAC) Meeting, Feb 26-27, 2015, Bethesda, MD.
16. N. Meethong, H.-Y. Huang, W. C. Carter, Y.-M. Chiang, Electrochem. and Solid-State Lett. 10, A134 (2007).
17. N. Meethong, H.-Y. Huang, S. A. Speakman, W. C. Carter, Y.-M. Chiang, Adv. Func. Mater. 17, 1115 (2007).
18. N. Meethong, Y.-H. Kao, S. A. Speakman, Y.-M. Chiang, Adv. Func. Mater. 19, 1060 (2009).
19. Y.-H. Kao, M. Tang, N. Meethong, J. Bai, W.C. Carter, Y.-M. Chiang, Chem. Mater. 22, 5845 (2010).

Period of Performance 9/15/2012 - 9/14/2015

During the performance period, we investigated the nonequilibrium response of model systems of low and high electrochemical strain, illustrated in Figure 1, and in essence "bookended" the range of behavior. In each instance, the response referred to occurs in micro- to nanoscopic particle systems; at larger crystal size scale, even modest transformation strains are typically accommodated by brittle fracture, and furthermore the electrochemical kinetics are typically too slow to be of interest in practical devices. In the Li-phospho-olivine system $Li(Mn,Fe)PO_4$, the transformation strain can be tuned over a range from ~1 vol% to ~6.5 vol% by varying the transition metal ratios, as a consequence of which distinctly different responses are obtained, as discussed below. We believe that plasticity plays a relatively minor role in these crystal systems at transformation strains below ~5%. At the other extreme, under the previous award we also studied lithiated Si, in which the electrochemical strain exceeds 300% and amorphization is an established response. In this case plastic deformation of the resulting alloy dominates the response to electrochemical strain. We showed that this response and can be controlled in a manner that dictates the anisotropy and uniformity of electrochemical expansion and can mitigate mechanical failure [1,2].

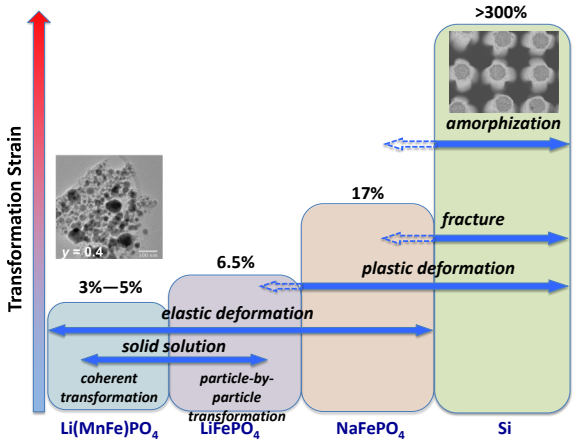

Figure 1. Systems studied, corresponding transformation strains, and nonequilibrium responses observed.

The intermediate regime of transformation strain in Fig. 1 is exemplified by $NaFePO_4$ (NFP) olivine, a new cathode compound with technological potential for sodium ion batteries. This compound's 17 vol% transformation strain is one of the largest amongst alkali ion intercalation cathodes. It is difficult to conceive of strain accommodation without plasticity, especially given the relatively high Young's modulus (~70 GPa) of olivines. We show below new results (to be published) that point to a unique and remarkable disordering response to electrochemical lithiation in nanoscale NFP. Understanding behavior in this intermediate strain regime, where plasticity must be included, is a major objective of the proposed research.

Non-Equilibrium Electrochemical Transformations in Phospho-Olivines

The phospho-olivine family $AMPO_4$ (A=Li, Na and M=Fe, Mn, Ni, Co), spans a wide range transformation-induced misfits, with free-strain values varying from as low as 1 vol% for $LiMn_{0.4}Fe_{0.6}PO_4$ to 6.5 vol% for $LiFePO_4$ to 17 vol% for $NaFePO_4$. Under the previous award we conducted experiments which revealed that room temperature phase transitions occur by quite different mechanisms as the transformation strain increases. Figure 2 shows a bird's-eye view of the (200) reflection in three olivine compositions during *operando* SR-PXD of an electrochemical cell (methodology developed in collaboration with the Structural Science Group, X-ray Science Division, at APS led by Dr. P. Chupas). It is immediately clear that the evolution of phase quantity (relative intensity) and composition (peak shift) follows a different path in each instance. Taking first the prototypical olivine, $LiFePO_4$ (LFP), Fig. 2 (left panel) shows what might be regarded as a "simple" first-order reaction with lattice strains whereby LFP is replaced by $FePO_4$ (FP) during charge, and vice versa on discharge. There is a size scale dependence on the phase content of individual electrode particles. Larger (~micron) particles can be composed of two-phases, whereas nanoscale particles having binary states [3], are either fully lithiated or fully delithiated (to within the solid solution limits of the endmember compounds $FePO_4$ and $LiFePO_4$; we have shown that the limiting compositions are also particle size dependent [4]). However, Fig. 2 shows that the behavior of LFP does not apply to the olivines in general. For example, in $LiMn_yFe_{1-y}PO_4$ (LMFP), the second-generation olivine of greatest commercial interest (due to its higher voltage and power), the *operando* SR-PXD shows a continuous transformation path through metastable solid solutions and phases (Figs. 2 and 3). We determined precisely the unit cell parameters of all crystalline phases during electrochemical titration, and find within the LMFP compositions three features that indicate nonequilibrium behavior: (a) During two-phase coexistence, the lattice dimensions, and therefore composition, of one or both phases change continuously, in violation of the Gibbs equilibrium phase rule; (b) Significant hysteresis is observed between charge and discharge in the compositions of phases at the same overall Li concentration (i.e., state-of-charge), and clearly both cases cannot represent the equilibrium condition; (c) The boundaries between phase fields (e.g., single and two-phase fields) differ between charge and discharge, and from literature phase diagrams [5,6]. From these results, it became clear that nano-LMFP does not follow the "binary particle" model of nano-LFP even when cycled slowly (C/20 rate) but instead exhibits continuous transitions within single particles--which we attribute to a thermodynamic tendency to minimize coherency strain energy. LMFP is unique in that the nonequilibrium solid solutions are stable for long periods (at least days) and occur uniformly throughout the material. This is explained by the low misfit strain between phases producing low coherency strain energy. In other work on LFP during the award period, we observed by TEM [7] that despite the large misfit strain,

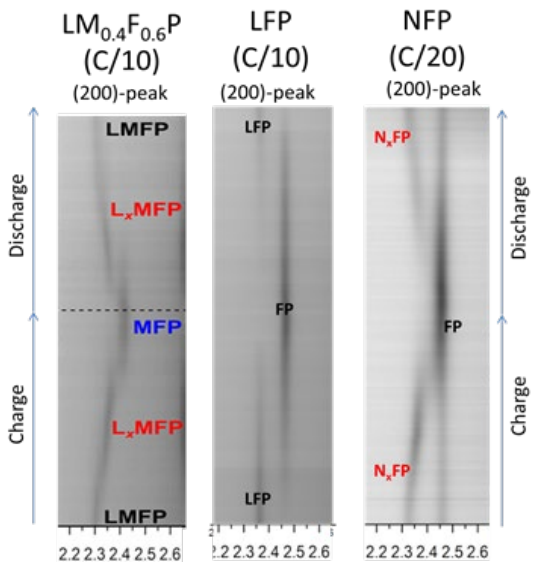

Fig. 2. SR-PXD results showing evolution of olivine (200) peak during a single charge-discharge (delithiation-lithiation or desodiation-sodiation). Peak shift and appearance indicate transformation behavior. All samples are synthesized by the same method and have nearly identical particle sizes (~50nm) and morphologies.

nanoscopic regions of solid solution do occur, but only at interfaces between lithiated and delithiated phase. At high current rates, recent X-ray results find evidence for solid solution in a fraction of LFP samples as well [8]. Such behavior is qualitatively explained by phase-field modeling by us in 3D (see Figure 9) and other groups in 2D [9], which reveals that misfit strain can thermodynamically suppress phase separation between FP and LFP and result in solid solution behavior upon (de)lithiation. We are conducting phase-field simulations to provide detailed prediction on the electrochemical and material conditions (e.g. applied overpotential or charge/discharge rate, electrode geometry, interface coherency etc) leading to observed solid solution behavior in LMFP, and to make quantitative comparison with experiments.

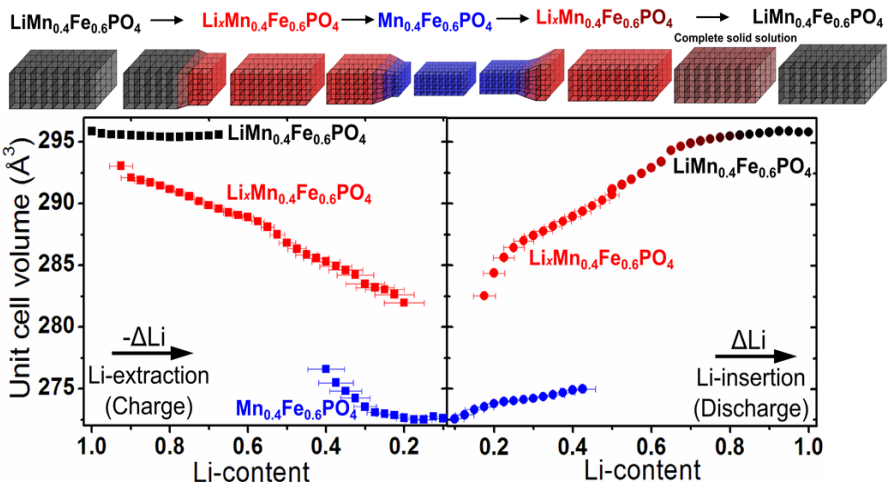

Fig. 3 . Unit cell volumes determined by Rietveld refinement of operando SR-PXD data measured during Li extraction (charge) and insertion (discharge) at a C/10 rate of LMFP (52 nm particles), supporting a coherent transformation model as shown at top. Sample has 52nm average crystallite size.

Coherency Strain as a Prerequisite for High Power

We subsequently utilized the tunable strain of LMFP to answer a key question: *Does low transformation strain, or access to a coherent phase transition, correlate to the exceptional power performance of olivines such as LMFP?* As we showed, LMFP delivers higher capacity at the C-rates above 10C than does nano-LFP. For this reason LMFP is of current commercial interest for high power Li-ion batteries for microhybrid (start-stop operation) and HEV applications, where its advantages over LFP are especially apparent at low use temperatures (so-called "cold crank"). The question of mechanism is not easily answered *a priori* since it is not known which atomic transport steps are rate-limiting for transformation mechanisms limited by migration of a coherent or incoherent interface. However, upon applying detailed *operando* structure analyses to samples of a range of Mn content (for which high power electrochemical properties have been measured by collaborators at A123 Systems LLC), we demonstrated a clear correlation (Figure 4). Here, the Rietveld-refined transformation strain measured during discharge is plotted against Mn content between pure LFP (y = 0) and Mn concentration of y = 0.8. The background contours (in blue) show the discharge capacity for each composition at C-rates from C/5 (12 min discharge) to 50C (1.2 min discharge). Each LMFP composition has two first-order transitions corresponding to the Fe^{2+}/Fe^{3+} couple and the Mn^{2+}/Mn^{3+} couple, with an intermediate solid solution phase existing between the endmembers. In Fig.4a, the broad maximum for high C-rate correlates with small misfit strains (<3 vol%). Indeed, the y = 0.2 composition near the maximum is unique in that the first order transition is completely bypassed during (nonequilbrium) discharge (Fig. 4b) but not charge. Figure 4 shows only volumetric strains; however, the minimum linear strains occur along the c axis and the minimum area strains within the bc plane. At high power, the critical volume strain is ~3%, and the linear and area strains are 0.1% and 1.2%. While transformation strain plays an important role in suppressing phase separation, quantitative prediction of the optimal composition and rate

capability of LMFP is non-trivial. Our experience with modeling LFP shows that the phase boundary orientation and hence misfit strain vary with discharge/charge rate, and complete solid solution behavior only occurs above an overpotential of ~80mV when the elastic energy penalty associated with the large misfit strain of (010) phase boundary can be overcome. Furthermore, the effect of coherency strain on the rate capability of L*M*P has two opposing effects: while it thermodynamically reduces or eliminates the two-phase co-existence region, kinetically it represents an energy barrier to phase transition and Li intercalation. Therefore an optimal transformation strain exists, which is both material and rate dependent, to maximize rate performance. Our phase-field model of LFP can be extended to LMP to predict the relation between coherency strain, the ability to bypass first-order transition and the Li intercalation kinetics in this system, and to provide useful insights on how to optimize material compositions for different application conditions.

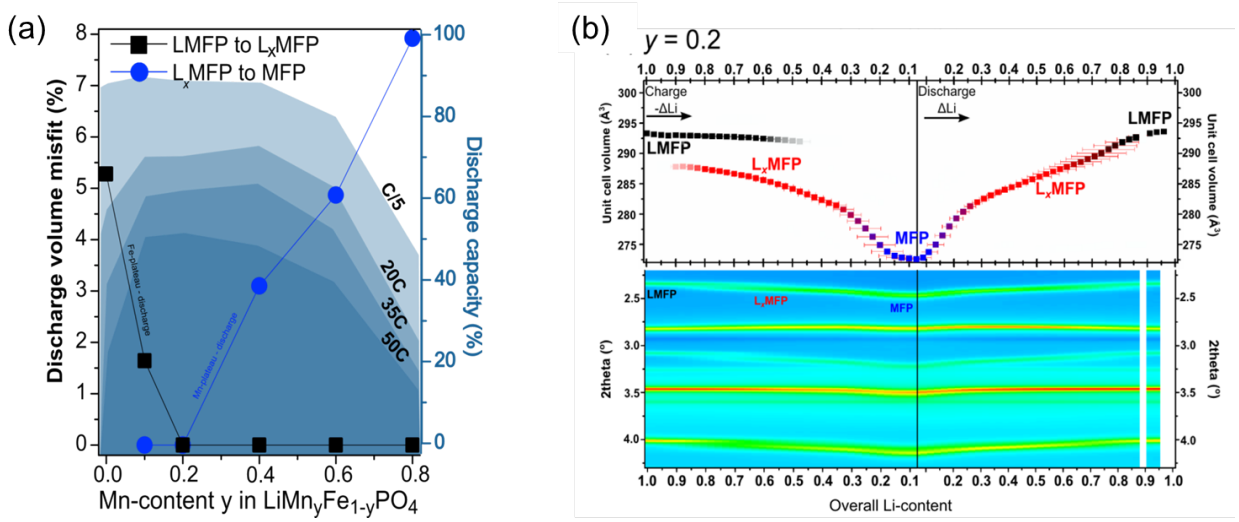

Figure 4. a) Volume misfit strain observed during operando discharge for LMFP, vs. Mn content. Shaded contours show the discharge capacity measured at C-rates from C/5 up to 50C. b) Unit cell dimensions for y = 0.2 sample during a charge/discharge cycle at C/10 rate. A small-strain first-order transition during charge is completely bypassed during discharge, producing a continuous solid solution transition.

Novel Electrochemically-Induced Phase Behavior in $NaFePO_4$

Sodium-ion batteries are of much interest as an alternative to Li-ion due to the potentially lower cost of storage (i.e., $/kWh) associated with greater natural abundance of Na vs. Li. However, the energy density of Na-ion is typically lower for isostructural hosts due to the ~20% lower insertion potential of Na. Consequently, use of hosts based on low-cost transition metals such as Fe and Mn are essential if the cost advantages are to be realized. Sodium olivines are therefore of interest for much the same reasons as lithium olivines. However, pure $NaFePO_4$ is not stable in the olivine structure but instead forms maricite, which is largely electrochemically inactive. Nonetheless, the properties of metastable olivine NFP can be studied in samples prepared from $LiFePO_4$ by chemical delithiation followed by electrochemical sodiation.

Here, we prepared NFP in this manner: using starting $LiFePO_4$ powders of ~50nm equivalent spherical particle size that were synthesized identically to those we previously used over a decade of studying pure and doped LFP [4,10,11,12,13,14]. ICP analysis showed that the NFP we prepared had less than 1% residual Li. This approach allows us to compare phase behavior of NFP that is *morphologically identical* to our LFP and LMFP samples (Fig. 2). Using the same AMPIX *operando* cell for SR-PXD at APS, the olivine NFP phase behavior during electrochemical sodiation (discharge) and desodiation (charge) at C/20 galvanostatic rate was observed. Careful structure refinement led to the results shown in Figure 5. Fig. 5a shows the voltage vs. Na/Na^+ during initial sodiation (discharge) of the chemically delithiated starting olivine $FePO_4$ followed by a complete charge-discharge curve. The cell voltage shows hysteresis between discharge and charge, and exhibits a single characteristic voltage on discharge but two voltage "plateaus" on charge that suggest a pair of two-phase equilibria, followed by a continuously rising voltage in a single solid solution regime. Figure 5b shows the corresponding unit cell volumes of the highly sodiated $Na_{1-y}FePO_4$ ($0<y<\sim0.4$) and highly desodiated Na_xFePO_4 ($0<x<0.08$) olivines, which are the only crystalline phases detected. (A separately determined Vegard's relationship allows the Na content to be determined from the unit cell parameters.)

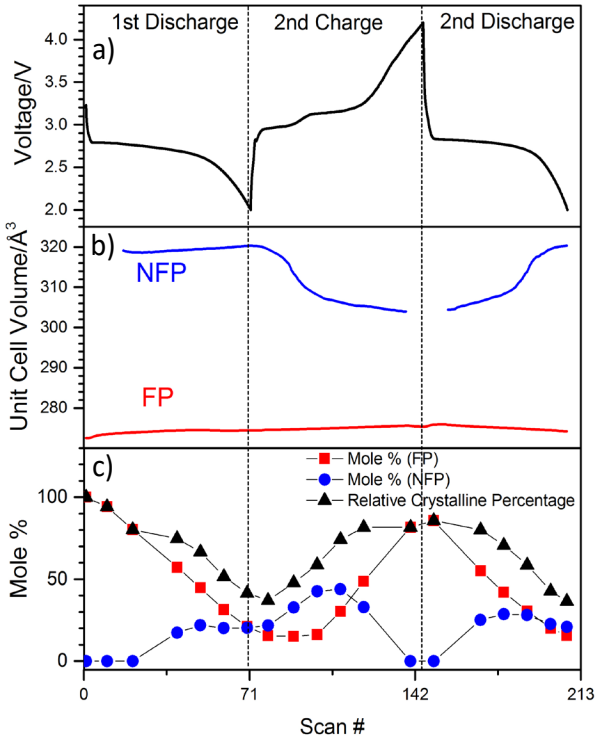

Fig. 5. Operando cell results for olivine $NaFePO_4$ vs. Li/Li^+. (a) Reversible sodium insertion into chemically delithiated $LiFePO_4$ of 50nm average crystallite size at C/20 rate, reaching 90% of the theoretical capacity. Note difference in behavior between first insertion and subsequent cycle. (b) Unit cell volume for the highly sodiated and nearly desodiated olivine phases, and (c) Variation in individual and total crystalline phase content with electrochemical cycling.

The unit cell volumes are approximately invariant during the 1st discharge (sodiation), suggesting a conventional first order transition. However, during the 2nd charge (desodiation), the unit cell volume of the NFP decreases following an S-shaped curve, and during the 2nd discharge this S-shaped curve is approximately reversed. The difference in unit cell volume between the sodiated and desodiated coexisting olivine phases is large and variable, ranging from 16% to 10%, which is greater than known for any other olivine.

Upon quantifying the SR-PXD data for the absolute amount of each crystalline phase across the electrochemical cycles (Fig. 5c), additional clues emerge. Fig. 5c plots the relative amount of each olivine phase, and the total amount of crystalline phase, as a function of scan number (proportional to Na content). During first sodiation, the total crystalline fraction decreases to 60% of its initial value, and upon desodiation only about 90% of the crystalline content is recovered. From the 2nd charge/discharge cycle, this behavior appears to be largely reversible. Clearly, one or more disordered phase must be created upon cycling. (Analysis of literature data for NFP [15] suggests that similar behavior may have been seen previously but was not recognized by the researchers.) However, no significant increase in background diffraction was

detectable probably because the integrated intensity of crystalline peaks is small compared to total diffraction intensity.

This electrochemically-induced disorder is counter to expectations, for the following reasons. It is known that $FePO_4$ can form an amorphous phase. The stable structure of $FePO_4$ when synthesized at 1 atm pressure is not olivine but quartz; $FePO_4$ may be thought of as a "II-IV" analog of SiO_2. In previous work under this award we found evidence for amorphization upon delithiation of $LiFePO_4$ towards the $FePO_4$ composition. What is striking about the present results is that we *begin* with $FePO_4$ and observe disorder *upon sodiation*. It has been observed that chemically-synthesized amorphous $FePO_4$ exhibits partial crystallization upon repeated insertion of alkali ions [16], which is also counter to the present observations. It is difficult to imagine any phase configuration in which a crystal-crystal transformation strain of 10-16 vol% could be accommodated without plasticity, especially given that the orthorhombic olivine structure is low-symmetry and there are no obvious ferroelastic accommodation mechanisms. Dislocation plasticity may also be difficult to induce given the large Burger's vectors inherent to olivine. We therefore believe that the observed disorder/amorphization occurs as a response to the large induced transformation strains, in effect facilitating plasticity. This novel response of NFP makes it a valuable model to bridge the behavior to that of the low-transformation strain olivines and silicon, discussed next.

Silicon: Example of Electrochemically-Induced Phase Transformations with Plasticity

Plasticity becomes increasingly important as the Vegard's strains during electrochemical storage increase. Perhaps no system better exemplifies the potential for enormous storage capacity while also requiring accommodation of enormous transformation strains than silicon anodes. A key issue in the application of Si as Li battery electrodes is its pulverization caused by the substantial volume expansion (~300%) upon Li insertion. Recent experiments reveal that c-Si undergoes strongly anisotropic volume expansion upon lithiation [17,18], which results in stress concentration and fracture and thus has significant implications for the structural integrity of Si electrodes. To develop strategies to mitigate mechanical failure, it is important to obtain a fundamental understanding of the relation between phase boundary movement, plastic flow and electrode morphology evolution in Si. A few models [18-20] have been proposed to explain the observed anisotropic swelling behavior, but they face limitations in several aspects, and most notably, in the difficulty to connect model parameters with experimental quantities and to perform large-scale, three-dimensional simulations due to the high computational cost associated with them.

During the previous performance period, we developed a mesoscale model for simulating concurrent interface-limited phase transformation and large plastic deformation in crystalline Si (c-Si) upon lithiation. This model is briefly reported in ref. 1. Ref. 2 provides a detailed exposition of the model and its application to the morphological design of c-Si anodes was submitted and under revision. Our model uses a front-tracking method to simulate phase boundary motion. It overcomes the limitations of previous models and allows key model parameters to be directly evaluated from experiments or atomistic calculations. In particular, the anisotropic mobility *M* of the phase boundary between c-Si and amorphous Li_xSi is expanded into a series of polynomial functions of interface orientation $\vec{n} = \{n_1, n_2, n_3\}$ invariant under cubic symmetry:

$$M(\vec{n}) = A_1 I_1(\vec{n}) + A_2 I_2(\vec{n}) + A_3 I_3(\vec{n}) + A_4 I_3(\vec{n})^2 + \cdots$$

where coefficients $\{A_j\}$ can be assessed by measured or calculated interface velocities of different crystal planes [**Error! Reference source not found.**,**Error! Reference source not**

found.] and the I_i are polynomial functions that have cubic point group symmetry. Plastic deformation and volume expansion in the amorphous Li_xSi is modeled by the large deformation theory with numerical implementation in ABAQUS finite element software.

The model was first validated based on its ability to simulate the lithiation-induced shape change of c-Si nanopillars/nanowires of different crystallographic orientations with good agreement with experimental observations, as shown in Figure 6(a). The very efficient numerical algorithm also enables us to simulate for the first time the shape evolution of a three-dimensional Si particle upon lithiation, showing very good agreement (Figure 6(b)) with experiment [21]. An important insight we gained from the simulations is that anisotropic volume change in Si upon Li insertion can induce plastic necking instabilities, which results in strain concentration and crack initiation at the surface (Figure 6(c)).

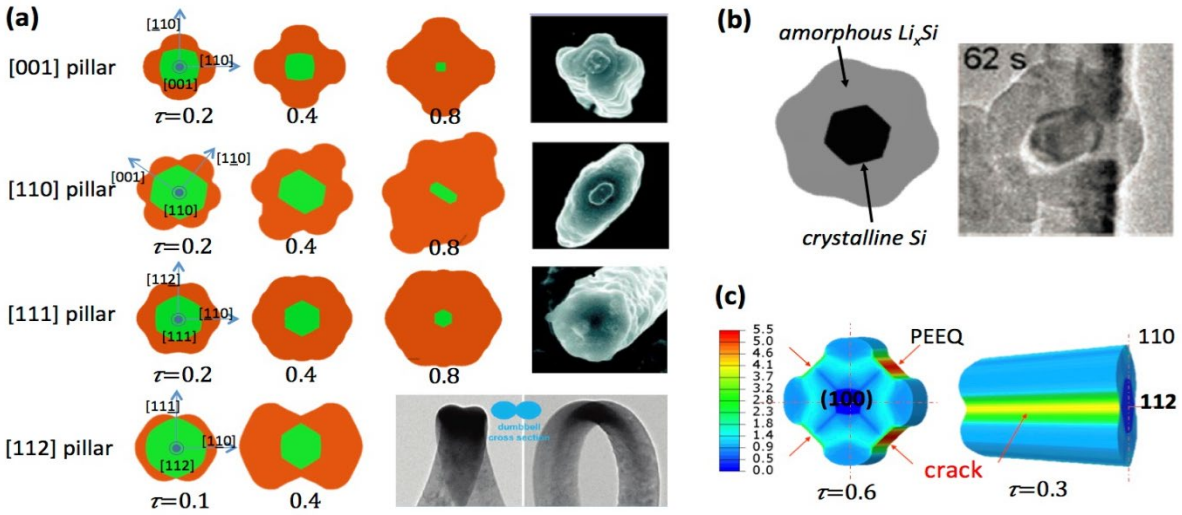

Figure 6. (a) Simulated morphological evolution of a circular Si pillar with [001], [110], [111] and [112] orientation and comparison with experimental observations adapted from refs. 17,18. Green color represents c-Si core and orange is amorphous Li_xSi shell. τ is normalized simulation time. (b) Simulated morphology of a partially lithiated spherical Si particle viewed along [111] axis (left) vs. experimental image (right, adapted from ref.21). (c) Illustration of computed strain concentration and likely crack initiation sites on the surface of [001] and [112] pillars.

Nanoscaling of electrode structures has yielded substantial progress in suppressing lithiation-induced fracture and improving cycle life of Si anodes. However, nanostructured Si electrodes face challenges in high cost, relatively low packing density of active material, and safety risks due to high solid/electrolyte interface reaction rates, which adversely affect their applications in commercial of Li batteries. Using our model as an exploratory tool, we demonstrated a novel strategy to accommodate plastic flow and mitigate fracture in Si through *morphological design*. This approach could lead to the development of fracture-resistant Si micro-electrodes to avoid the drawbacks of nanostructures. The key underpinning of our strategy is to offset the anisotropy in volume expansion with a proper anisometric shape of Si anode to produce a much more uniform volume expansion. Based on the observation that the swelling of amorphous Li_xSi is the largest along crystallographic directions where the crystalline/amorphous phase boundary has the highest mobility, we propose a simple design rule to determine the optimal anisometric morphology of a silicon pillar: *the pillar cross section should be a polygon bound by planes*

corresponding to the largest (and second largest if necessary) local maxima of interface mobility, and the distance from each side to the polygon center should be proportional to the mobility of that side.

Figure 7(a) shows an as-designed [100] pillar with a square cross section and four <011> edges. Simulation of the lithiation of this pillar clearly exhibits its advantages over a circular pillar. As shown in Figure 7(a)-(b), though initially anisometric, the square pillar obtains a highly isometric cross section after a transient period while the circular pillar shows an opposite trend. Throughout the lithiation process, the square pillar has much lower plastic strain concentration on surface (Figure 7(c)) due to the more isotropic swelling behavior. Similar improvement is also seen in the simulation of Si pillars with other crystallographic orientations after their cross sections switch to the designed anisometric shapes.

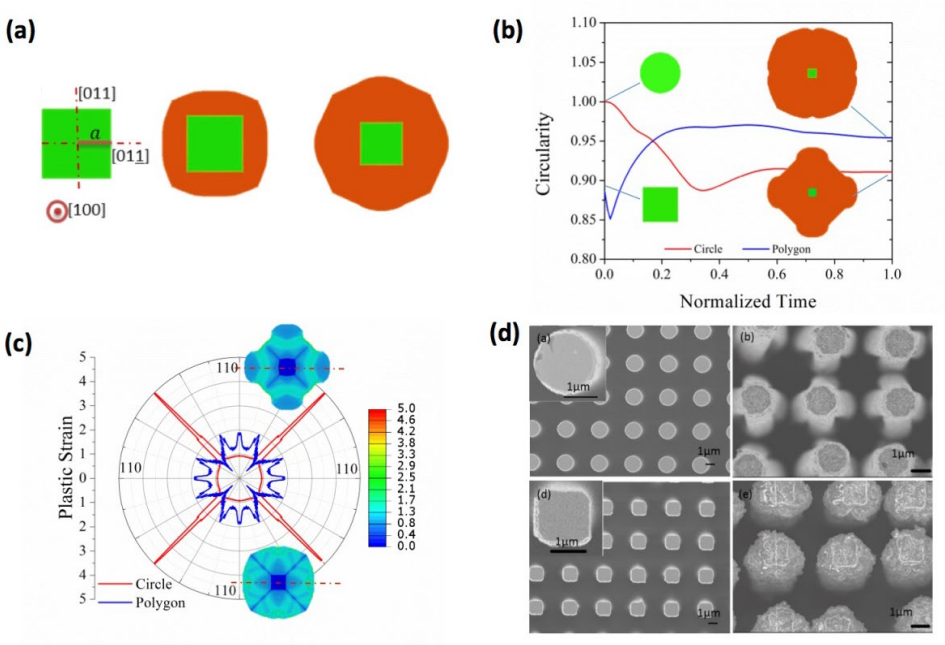

Figure 7 (a) Simulated morphological evolution of a square [100] Si pillar. (b) Evolution of the circularity of [100] pillars with the designed square (blue) and circular (red) cross sections upon lithiation. (c) Equivalent plastic strain distribution on the surface of [100] square (blue) vs circular (red) pillars. (d) Experimental verification of the predicted shape change of [100] pillars with circular (top) and designed square (bottom) cross sections.

The effectiveness of our proposed electrode morphologies was validated by experiments on Si micropillars fabricated using photolithography techniques [2]. The experiment shows uniform volume expansion of pillars with the optimal cross section, as predicted by the model (Figure 7(b)). It is also observed [1] that while cracks already form in circular [100] pillars at a volume expansion of ~50% upon lithiation, they are not found in [100] square pillars until a much later stage of ~150% volume expansion. The crack length also grows more slowly with the degree of lithiation. These results verify that morphological control is a useful approach to accommodating plastic deformation and suppressing fracture in microsized silicon anodes. Such a strategy should also be applicable to other high transformation strain systems such as NFP.

References

1. Ye, J. C. , An, Y. H., Heo, T. W., Biener, M. M., Nikolic, R. J., Tang, M., Jiang, H., Wang, Y. M., J. Power Sources 2014, 248, 447.
2. Y. An, B.C. Wood, J. Ye, Y.-M. Chiang, Y.M. Wang, M. Tang, H. Jiang, "Improving the Fracture Resistance of Crystalline Silicon Electrode by Morphological Design," in revision.
3. Chueh, W. C., El Gabaly, F., Sugar, J. D., Bartelt, N. C., McDaniel, A. H., Fenton, K. R., & McCarty, K. F., *Nano Lett.* 2013, 13, 866.
4. Meethong, M., Huang, H.-Y., Carter, W.C., Chiang, Y.-M., *Electrochem. Solid-State Lett.* 2007, 10, A134.
5. Yamada, A., Kudo, Y., Liu, K.-Y., *J. Electrochem. Soc.* 148, A1153 (2001).
6. Malik, R., Zhou, F., Ceder, G. *Phys. Rev. B* 79, 214201 (2009).
7. Niu, J., Kushima, A., Qian, X., Qi, L., Xiang, K., Chiang, Y.-M., and Ju Li, *Nano Lett.* 2014, 14, 4005.
8. Liu, H., Strobridge, F.C., Borkiewicz, O.J., Chapman, K.W., Chupas, P.J., and Grey, C.P., *Science* 2014, 344, 1252817.
9. Cogswell, D. A., and Bazant, M. Z., *ACS Nano* 2012, 6, 2215.
10. Tang, M., Carter, W. C., Chiang, Y.-M., *Annu. Rev. Mater. Res*. 2010, 40, 501.
11. Kao, Y.-H., Tang, M., Meethong, N., Bai, J., Carter, W.C., Chiang, Y.-M., *Chem. Mater*. 2010, 22, 5845.
12. Ravnsbæk, D. B., Xiang, K., Xing, W., Borkiewicz, O. J., Wiaderek, K. M., Gionet, P., Chapman, K. W., Chupas, P., Chiang, Y.-M., *Nano Lett.* 2014, 14, 1484.
13. Meethong, N., Kao, Y.-H., Tang, M., Huang, H.-Y., Carter, W.C., Chiang, Y.-M., *Chem. Mater*. 2008, 20, 6189.
14. Meethong, N., Kao, Y.-H., Speakman, S.A., Chiang, Y.-M., *Adv. Funct. Mater.* 2009, 19, 1060.
15. Galceran, M., Saurel, D., Acebedo, B., Roddatis, V. V., Martin, E., Rojo, T., Casas-Cabanas, M., *Phys. Chem. Chem. Phys.* 2014, 16, 8837.
16. Mathew, V., Kim, S., Kang, J., Gim, J., Song, J., Baboo, J. P., Park, W., et al., *NPG Asia Mater.* 2014, 6, e138. DOI:10.1038/am.2014.98.
17. Lee, S. W.; McDowell, M. T.; Choi, J. W.; Cui, Y. *Nano Let.* 2011, 11, 3034-3039.
18. Liu, X. H.; Zheng, H.; Zhong, L.; Huan, S.; Karki, K.; Zhang, L. Q.; Liu, Y.; Kushima, A.; Liang, W. T.; Wang, J. W.; Cho, J. H.; Epstein, E.; Dayeh, S. A.; Picraux, S. T.; Zhu, T.; Li, J.; Sullivan, J. P.; Cumings, J.; Wang, C. S.; Mao, S. X.; Ye, Z. Z.; Zhang, S. L.; Huang, J. Y. *Nano Lett.* 2011, 11, 3312-3318.
19. Yang, H.; Huang, S.; Huang, X.; Fan, F. F.; Liang, W. T.; Liu, X. H.; Chen, L. Q.; Huang, J. Y.; Li, J.; Zhu, T.; Zhang, S. L. *Nano Lett.* 2012, 12, 1953-1958.
20. Yang, H.; Fan, F.; Liang, W.; Guo, X.; Zhu, T.; Zhang, S. *J. Mech. Phys Solids* 2014, 70, 349-361.
21. McDowell, M.T.; Ryu, I.; Lee, S.W.; Wang, C.; Nix, W.D.; Cui, Y. *Adv Mater.* 2012 24, 6034.

Period of Performance 9/15/2015 - 9/14/2018

During the period of performance, the following questions were addressed:

(i) How does the magnitude of the phase transformation strain, and the magnitude of the electrochemical driving force, dictate the phase transformation pathway? Our approach takes advantage of a unique series of carefully curated olivines samples developed over more than a decade. *Operando* synchrotron X-ray diffraction, pair distribution function (PDF) analysis and high resolution TEM are used to characterize phase behavior under controlled electrochemical driving force. Phase-field and phase transformation models are used to identify transformation mechanisms and to interpret deviations from equilibrium transformation paths. Large deviations from equilibrium are found to be the rule rather than the exception.

(ii) What is the relationship between transformation strain and electrochemical performance? While it can be assumed that the rate-limiting kinetic steps and atomic species change with the transformation mechanism, it is not currently possible to predict electrochemical capacity and rate performance from basic structural knowledge. Systematic study of the olivine family makes such correlations possible for the first time.

(iii) What is the role of plasticity? While elastic response dominates at small strain while plasticity dominates at high strain, many materials of interest for energy storage fall in the middle – where strains are large enough that the elastic limit is surely exceeded, yet the parent/daughter phases remain structurally similar. The bridge between elastic and plastic response is being studied in this program experimentally and theoretically.

Results

1) Disorder as a Mechanism of Phase Transformation Strain Accommodation

Olivine $NaFePO_4$ (NFP), heretofore relatively unstudied, is of interest to this project as it is the intercalation compound (unlike silicon) with the largest volume change (17 %) across a first-order transition of any intercalation compound known to us. Over the past year, we have elucidated how strain is accommodated in NFP using a combination of experimental techniques including *operando* SR-PXD, pair distribution function (PDF) analysis as well as transmission electron microscopy (TEM). Figure 1(A) compares NFP to materials previously studied under this program. Figure 1 (B) displays *operando* SR-PXD data for a $FePO_4$/Na half-cell undergoing charge and discharge; the horizontal axis is the Na content (from 212 PXD scans).

During the first discharge (first Na insertion, there is 20% decrease in the total crystalline phase percentage compared to the starting FP (Figure 1 (B), lower-left). During the second charge (desodiation), further loss of crystallinity occurs,

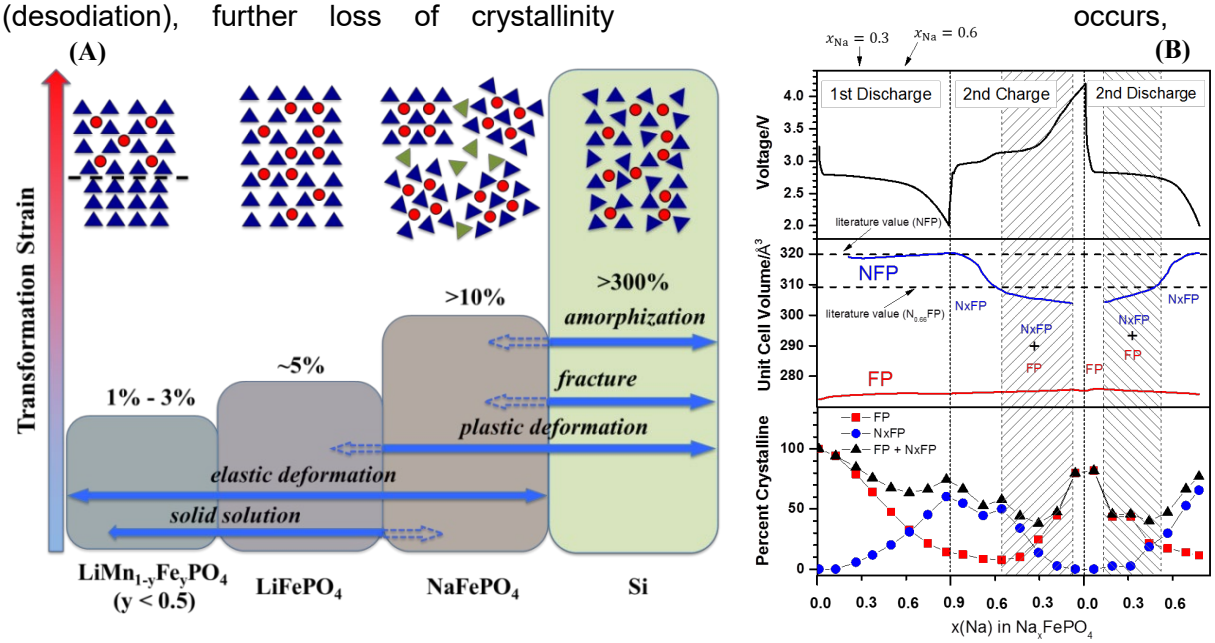

Figure 1 (A) Systems studied, corresponding transformation strains, and phase transformation behaviors observed. Voltage profile of sodium iron phosphate cell (B – upper), refined unit cell volume of observed crystalline phases (B – middle) and calculated mole percentage of crystalline phases against initial amount of crystalline FP phase (B – lower) obtained from *operando* PXD data.

especially across the two-crystalline-phase field (the shaded region). Formation of a disordered phase is implied, but the nature of this phase is not clear from the SR-PXD results alone. Thus we used pair distribution function (PDF) analysis (with colleagues at APS) to characterize the short-range order of the newly formed disordered phase. Two-phase and three-phase structure models were tested for PDF data of samples discharged to compositions x_{Na}=0.3 and x_{Na}=0.6, respectively. A satisfactory fit could not be obtained without addition of a third, amorphous phase, which interestingly has short-range order that can be fit with two domain parameters close to those of NFP, and a third parameter close to that of FP. These results suggest a unique strain-accommodation mechanism, not previously reported, wherein an amorphous phase is formed that is able to orient topotaxially against FP or NFP, forming coherent or semicoherent interfaces.

2) Mesoscale Nucleation and Growth in Multi-Particle Assemblies

A second important question addressed in this project is how nucleation and growth proceeds in large multiparticle ensembles appropriate to battery electrodes. A large set of electrochemical data from potentiostatic (PITT) measurements for nanoscale $LiMn_yFe_{1-y}PO_4$ was obtained and analyzed by the Johnson-Mehl-Avrami-Kolmogolov (JMAK) model.[1] While the JMAK analysis has been repeatedly applied to olivine cathodes in literature[2,3], its major assumptions (infinite system, homogeneous nucleation) are not satisfied by nanoscale particles, raising question for such an exercise. Here, we showed for the first time why such analysis can be valid for nanoparticulate systems, if it occurs within a mesoscopic system of secondary particles composed of nanoscale primary particles. We show that the Avrami exponent *n* can be generally expressed as $n = a + b*c$, where parameter *a* is related to nucleation kinetics (a=0, instantaneous nucleation; a = 1, constant nucleation rate), *b* represents the growth

dimensionality and *c* is controlled by phase boundary migration mechanism (diffusion- vs interface-limited). In $LiMn_yFe_{1-y}PO_4$ samples of varying Mn:Fe ratio and particle size, under different overpotentials and temperatures, we find that the Avrami exponent *n* systematically varies between 0.5 and 1.5 (Figure 2). These results lead to the following new insights:

1) Nucleation occurs through heterogeneous nucleation on two-dimensional particle surface followed by one-dimensional phase growth (i.e. *b* =1) into individual primary particles.
2) Phase boundary movement is controlled by Li diffusion, i.e. *c* = 1/2.
3) Variation of Avrami exponent indicates the variation in nucleation rate since *n* = *a* + *1/2* based on 1) and 2). Nucleation rate decays with time; the decay rate is directly correlated with a nucleation barrier modulated by particle size, composition, overpotential and temperature.

Complementary to the JMAK analysis is our recent discovery of a *hybrid-mode growth mechanism* during intercalation-induced phase transformations in secondary particles[4]. Delithiation of $LiFePO_4$ microrods during *operando* hard x-ray transmission microscopy (TXM) shows that growth of $FePO_4$ domains along (100)/(001) particle surface is much faster than the phase boundary movement into the particle, Fig. 3(A,B). Detailed analysis and phase-field simulation reveal that $FePO_4$ growth is governed by two distinct mechanisms along different directions: it is *surface-reaction-limited* (SRL) along [100] but bulk-diffusion-limited in the [100]/[001] direction. This observation provides the first direct confirmation of the SRL phase boundary migration mechanism, and also sheds light on how nucleation and growth may proceed in secondary particles. We propose that the SRL growth provides a deterministic mechanism for accelerating nucleation in inter-connected primary particles as the new phase can propagate rapidly between them through SRL growth once a nucleation event occurs in one particle. Our simulation predicts that the peak current observed in potentiostatic experiments corresponds to when nearly all the primary particles in a secondary particle are "activated" by fast SRL growth and start transforming as

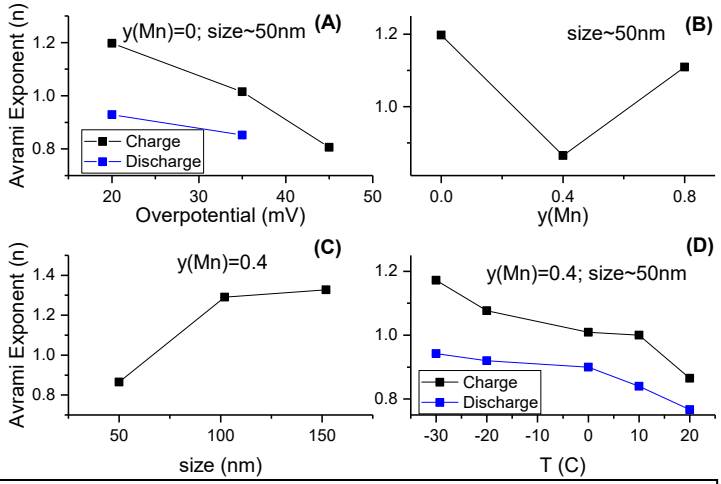

Figure 2. Effect of (A) applied overpotential, (B) Mn-content y(Mn), (C) particle size and (D) temperature on the Avrami exponent from fitting the JMAK equation to PITT measurement of nanoscale olivine $LiMn_yFe_{1-y}PO_4$.

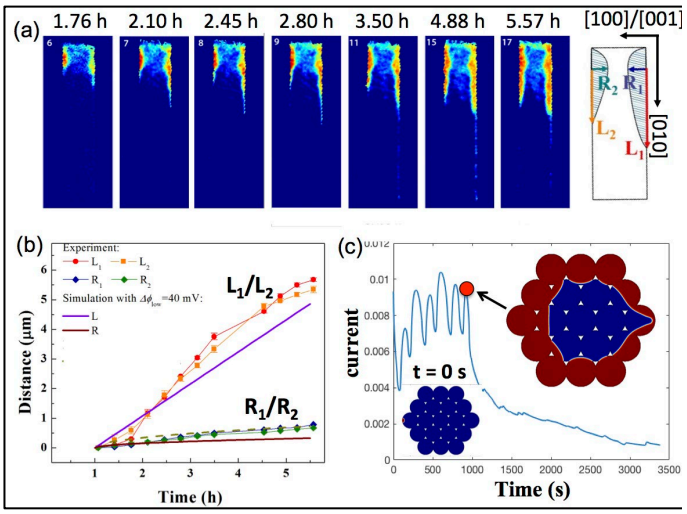

Figure 3 (a) Operando TXM chemical maps of the delithiation of a $LiFePO_4$ microrod. Red – $FePO_4$; Blue – $LiFePO_4$. (b) The [010] (square) vs [100]/[001] (diamond) dimensions of $FePO_4$ domains compared against simulation (solid lines). (c) Current vs time upon delithiation of a 200nm secondary particle from phase-field simulation.

shown in Fig. 3(C). An important implication of this prediction is that the peak current time should scale with secondary particle size.

We further identified several additional intercalation compounds with unusually large volume or shear strain, in which the generality of the disordering response could be investigated. It is hypothesized that such *in-situ* disordered electrodes may have attractive electrochemical properties. For example, *operando* TXM experiments could be performed to directly image the nucleation and growth process in secondary particles to examine the JMAK interpretation of the PITT measurement and our model predictions. Future work could extend the theoretical study of the mesoscopic nucleation and growth kinetics in electrodes to consider the effect of misfit stress. Specifically, we hypothesize that stress-induced phase boundary morphology instability will occur in single crystalline and secondary particles.

References

1. Fanfoni, M., and M. Tomellini. "The Johnson-Mehl-Avrami-Kohnogorov model: a brief review." *Il Nuovo Cimento D* **1998**, *20*, 1171.
2. Allen, Jan L., T. Richard Jow, and Jeffrey Wolfenstine. "Kinetic study of the electrochemical $FePO_4$ to $LiFePO_4$ phase transition." *Chemistry of materials* **2007**, *19*, 2108.
3. Oyama, Gosuke, Yuki Yamada, Ryuichi Natsui, Shinichi Nishimura, and Atsuo Yamada. "Kinetics of Nucleation and Growth in Two-Phase Electrochemical Reaction of Li_xFePO_4." *The Journal of Physical Chemistry C* **2012**, *116*, 7306.
4. L. Hong, L. Li, Y.-K. Chen-Wiegart, J. Wang, F. Wang, K. Xiang, L. Gan, W. Li, F. Meng, J. Wang, Y.-M. Chiang, S. Jin, M. Tang, “Two-Dimensional Li Diffusion Behavior and Hybrid Phase Transformation Kinetics in Olivine Lithium Iron Phosphate ($LiFePO_4$)”, under review.

Period of Performance 9/15/2018 - 9/14/2020

During this period of performance, a no-cost extension was granted for minor remaining funds in our award in order to investigate ion-conducting compounds (i.e., solid electrolytes) in which structure and phase transitions are central to the physical properties of interest. Specifically, the work focused on cluster-based anti-perovskite compounds [1-3] for which first-principles calculations (including DFT and MD) at Virginia Commonwealth University (PI: Puru Jena) have been performed, and suggested the possibility of fast ion transport as well as other novel properties. These cluster-ion anti-perovskites have the general formula Li_3AX or Na_3AX in which A=O,S and X=AlH_4, BH_4, BF_4. X can also include partial substitution with the halogens Cl, Br and I, for which anti-perovskite formulations have previously been established. None of the computed cluster-ion anti-perovskites have previously been synthesized experimentally. Thus the main scope of this effort was to establish synthesis methods for anti-perovskites containing specific cluster-ions of interest, and if successful, to characterize their phase stability and transport properties.

Results

The hygroscopic nature common to all of the anti-perovskites in this compositional family, combined with the fact that a number of the starting materials are known strong oxidizers, dictated that all synthesis experiments should be conducted completely within an argon-filled glove box (~0.1 ppm partial pressure each of oxygen and water), including heat treatments. For some starting materials, violent exothermic reactions were observed upon mixing or heating to <250°C in the inert gas environment; see *Safety Note* at the end of this report.

Previously, successful synthesis of three cluster-ion anti-perovskites have been reported in the literature: Na_2NO_2 [4], Na_3OCN [4], and $Na_2(NH_2)(BH_4)$ [5]. In the present work, we attempted the synthesis of 31 compounds of anti-perovskite stoichiometry. Figure 1 displays the successful/unsuccessful attempts, plotted against the highest phase purity obtained in the samples, characterized on the basis of Rietveld refinement of powder X-ray diffraction data. We were able to confirm the synthesis of Na_2NO_2 and $Na_2(NH_2)(BH_4)$ using similar methods as reported in the literature (Na_3OCN was not attempted). In addition, five new cluster-ion anti-perovskites were synthesized. As shown in Figure 1, a high level of phase purity (>85%) was observed ion all of the successfully synthesized compounds (in some cases, after multiple experiments with systematic improvements in method). More than 20 compositions of the anti-perovskite stoichiometry were attempted that did not crystallize in the anti-perovskite structure. Several trends were observed, as noted below.

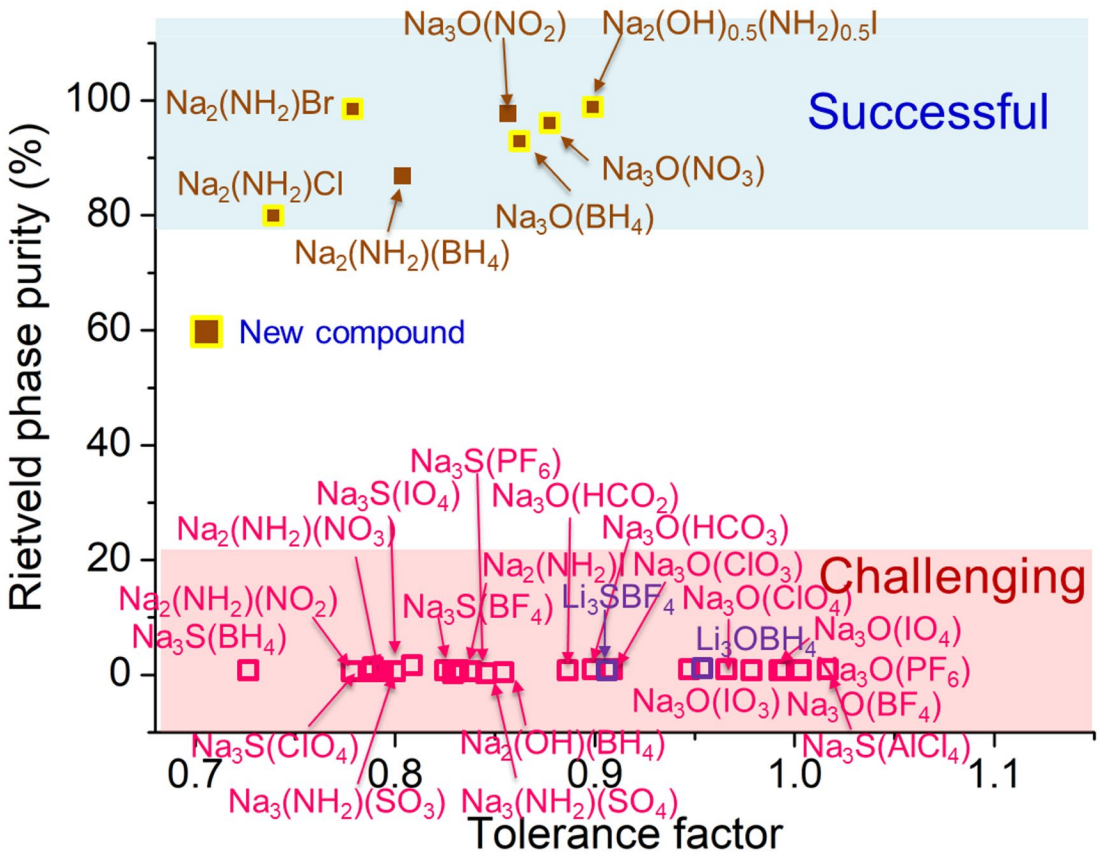

Figure 1. Summary of results for 31 attempted syntheses of cluster-ion anti-perovskites, plotted as anti-perovskite phase purity (from Rietveld refinement of powder XRD) against the computed Goldschmidt tolerance factor of the compound.

In all cases, we used a precursor containing the cluster ion of interest as a starting material in the synthesis reaction: $LiBH_4$, $NaBH_4$, $NaNH_2$ or $NaNO_2$. The synthesis temperatures ranged from 140°C to 260°C. No Li-based cluster-ion anti-perovskites were successfully synthesized using $LiBH_4$, we attempted to produce the compounds described in refs. [1-3]. Below the decomposition of this precursor (275°C), no reactivity was observed (by XRD); near and above its decomposition temperature, Li_3B was observed in all three cases. Li_3B is a known decomposition product of $LiBH_4$. Alternative Li salts and potentially hydrogen atmosphere may be required to stabilize compositions containing both Li and BH_4.

In contrast, all of the 5 new compounds synthesized to date are in the Na family, and include the anions NO_2, NH_2 and BH_4. Two include the BH_4 anion, $Na_3O(BH_4)$ and Na2(NH2)(BH4), and were synthesized using NaBH4 as a starting component. We believe that success with this precursor compared to LiBH4 may be associated with the greater stability of $NaBH_4$ (decomposition temperature 300°C); these two anti-perovskites were synthesized at 220°C. The remaining Na cluster-ion anti-perovskites were synthesized using $NaNH_2$ or $NaNO_2$ as a precursor. An example of an XRD pattern for $Na_3O(BH_4)$ at >99% phase purity is shown in Figure 2.

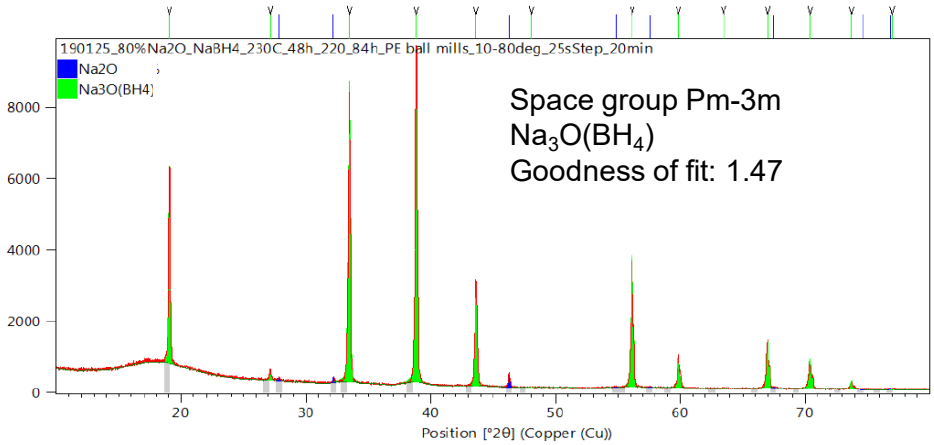

Figure 2. Powder X-ray diffraction pattern for $Na_3O(BH_4)$ showing >99% phase purity.

The successful synthesis of several cluster-ion anti-perovskites is promising, but does not yet allow direct comparison with the first principles modeling, which has to date focused on the Li family. In future work, alternative Li precursors are necessary, and some were identified. Conversely, calculations should be conducted for those anti-perovskites that have been successfully synthesized in the Na family, seeking similar structure-property correlations. Given the prevalence of light elements in all of these compounds, neutron diffraction is necessary for more detailed characterization of structure. Finally, the characterization of melting behavior could determine those compounds that are congruently-melting, and melt-based single crystal growth could be attempted.

References

1. Fang, Hong, Shuo Wang, Junyi Liu, Qiang Sun, and Puru Jena. "Superhalogen-based lithium superionic conductors." Journal of Materials Chemistry A 5, no. 26 (2017): 13373-13381.
2. Fang, Hong, and Puru Jena. "Sodium Superionic Conductors Based on Clusters." ACS applied materials & interfaces 11.1 (2018): 963-972.
3. Fang, Hong, and Puru Jena. "Li-rich antiperovskite superionic conductors based on cluster ions." Proceedings of the National Academy of Sciences 114.42 (2017): 11046-11051.
4. Müller, Winfried, and Martin Jansen. "ONa3, Kristallstruktur und Natriumionenleitfähigkeit." Zeitschrift für anorganische und allgemeine Chemie 591, no. 1 (1990): 41-46.
5. Chater, Philip A., Paul A. Anderson, James W. Prendergast, Allan Walton, Vicky SJ Mann, David Book, William IF David, Simon R. Johnson, and Peter P. Edwards. "Synthesis and characterization of amide–borohydrides: New complex light hydrides for potential hydrogen storage." Journal of Alloys and Compounds 446 (2007): 350-354.

Publications

The following papers have been published citing support from this program:

1. Y.-H. Kao, M. Tang, N. Meethong, J. Bai, W.C. Carter, Y.-M. Chiang, "Overpotential-Dependent Phase Transformation Pathways in Lithium Iron Phosphate Battery Electrodes," *Chem. Mater.*, 22[21], 5845-5855 (2010). (**DOI:** 10.1021/cm101698b)

2. M. Tang, W.C. Carter, J.F. Belak, Y.-M. Chiang, "Modeling the Competing Phase Transition Pathways in Nanoscale Olivine Electrodes," *Electrochemica Acta*, 56, 769 (2010) (doi:10.1016/j.electacta.2010.09.027).

3. M. Tang, W. C. Carter, Y.-M. Chiang, "Electrochemically-Driven Phase Transitions in Insertion Electrodes for Lithium-Ion Batteries: Examples in Lithium Metal Phosphate Olivines," *Annu. Rev. Mater. Res.*, Vol. 40: 501–529 (2010) (doi: 10.1146/annurev-matsci-070909-104435).

4. D. B. Ravnsbæk, K. Xiang, W. Xing, O. Borkiewicz, K. Wiaderek, P. Gionet, K. Chapman, P. Chupas, W. C. Carter, Y.-M. Chiang, "Extended solid solution behavior and coherent transformations in nanoscale olivine cathodes" *Nano Letters* **2014**, *14*,1484–1491.

5. Z. Li, D. B. Ravnsbæk, K. Xiang, C. Carter, Y.-M. Chiang, "$Na_3Ti_2(PO_4)_3$ as a sodium bearing anode for high energy density aqueous rechargeable sodium-ion batteries", *Electrochem. Comm.* **2014**, *44*, 12–15**.**

6. J. Niu, A. Kushima, X. Qian, L. Qi, K. Xiang, Y.-M. Chiang, J. Li, "In situ observation of random solid solution zone in LiFePO4 electrode", *Nano Letters* **2014,** 14(7) pp. 4005-4010 DOI: 10.1021/nl501415b.

7. Z. Li, K. Xiang, W. Xing, C. Carter, Y.-M. Chiang, "Reversible Aluminum-Ion Intercalation in Prussian Blue Analogs and Demonstration of a High-Power Aluminum-Ion Asymmetric Capacitor", *Advanced Energy Materials* **2014**.

8. R. Amin, D.B. Ravnsbaek, Y.-M. Chiang, "Characterization of electronic and ionic transport in $Li_{1-x}Ni_{0.8}Co_{0.15}Al_{0.05}O_2$ (NCA)," *J. Electrochem. Soc.* **162**(7), A1163-A1169 (2015). doi: 10.1149/2.0171507jes

9. Y. An, B.C. Wood, J. Ye, Y.-M. Chiang, Y.M. Wang, M. Tang, H. Jiang, "Mitigating Mechanical Failure of Crystalline Silicon Electrodes for Lithium Batteries by Morphological Design," *Phys. Chem. Chem. Phys.*, .**17**, 17718-17728 (2015). DOI: 10.1039/C5CP01385B

10. S. Pongha, B. Seekoaon, W. Limphirat, P. Kidkhuntod, S. Srilomsak, Y.-M. Chiang, and N. Meethong, "XANES Investigation of Dynamic Phase Transition in Olivine Cathode for Li-Ion Batteries," *Adv. Energy Mater.*, **5** (15), (2015). DOI: 10.1002/aenm.201570086

11. D. B. Ravnsbaek, K. Xiang, W. Xing, O. Borkiewicz, K. Wiaderek, P. Gionet, K. Chapman, P. Chupas, M. Tang and Y.-M. Chiang, "Engineering the Transformation Strain in $Li(Mn_yFe_{1-y})PO_4$ Olivines for Ultrahigh Rate Battery Cathodes," *Nano Letters*, ASAP article, March 1, 2016. DOI: 10.1021/acs.nanolett.5b05146

12. Wenting Xing, Kai Xiang, Dorthe B. Ravnsbæk, Liang Hong, Ming Tang, Zheng Li, Karena M. Wiaderek, Olaf J. Borkiewicz, Kamila W. Chapman, Paul J. Chupas, Yet-Ming Chiang, "Accommodating High Transformation Strains in Battery Electrodes *via* Formation of

Nanoscale Intermediate Phases: *Operando* Investigation of Olivine $NaFePO_4$," *Nano Letters*, **17**(3), 1696-1702 (2017). DOI: 10.1021/acs.nanolett.6b04971

13. Hong Li, Linsen Li, Yuchen-Karen Chen-Wiegart, Jiajun Wang, Kai Xiang, Liyang Gan, Wenjie Li, Fei Wang, Jun Wang, Yet-Ming Chiang, Song Jin, Ming Tang, "Two-Dimensional Lithium Diffusion Behavior and Probable Hybrid Phase Transition Kinetics in Olivine Lithium Iron Phosphate," *Nature Comm.*, **8**:114 (2017) DOI: 10.1038/s41467-017-01315-8.

14. K. Xiang, K. Yang, W.C. Carter, M. Tang and Y.-M. Chiang, "Mesoscopic Phase Transformation Kinetics in Secondary Particles of Electrode-Active Materials in Lithium-Ion Batteries," *Chem. Mater.*, **30**[13], 4216-4225 (2018), DOI: 10.1021/acs.chemmater.7b05407.

15. A. R. Balakrishna, Y.-M. Chiang and W.C. Carter, "Li-diffusion accelerates grain growth in intercalation electrodes: A phase-field study," *Phys. Rev. Materials* , **3**, 065404 (2019). https://doi.org/10.1103/PhysRevMaterials.3.065404

16. Christian Christensen, Aref Mamakhel, Ananya Balakrishna, Bo Brummerstedt Iverson, Yet-Ming Chiang, Dorthe Ravensbaek, "Order-disorder transition in nano rutile TiO_2 anodes: A high capacity low volume change battery material," *Nanoscale*, **11**, 12347-12357 (2019). https://doi.org/10.1039/C9NR01228A

17. C. Henriksen, J.Mathiesen, Y.-M. Chiang, K. Jensen, D. Ravnsbæk, "Reducing transformation strains during Na-intercalation in olivine $FePO_4$ cathodes by Mn-substitution," *ACS Applied Energy Materials*, 2019, 2, 11, 8060–8067, https://doi.org/10.1021/acsaem.9b01560.

18. *Adapting SOCOM to an Electrified World*, Karen Swider-Lyons, Joshua Lamb, Yet-Ming Chiang, Chapter 18, pp. 253-266, in Strategic Latency for Special Operations Forces, eds. Z. S. Davis, F. Gac, C. Rager, P. Reinger, J. Snow, 2021, ISBN-978-1-952565-07-6 LCCN-2021901137 LLNL-BOOK-818513 TID-59693.

19. K. Kim, Y. Li, P.-C. Tsai, F. Wang, S.-B. Son, Y.-M. Chiang, D. Siegel, "Exploring the Synthesis of Alkali-metal Anti-perovskites," *Chemistry of Materials*, **34**[3] 947-958 (2022), https://doi.org/10.1021/acs.chemmater.1c02150